

# Origin of Enhanced Water Oxidation Activity in an Iridium Single Atom Catalyst

Xueli Zheng<sup>1†</sup>, Jing Tang<sup>1†</sup>, Alessandro Gallo<sup>2</sup>, Jose A. Garrido Torres<sup>2</sup>, Xiaoyun Yu<sup>1</sup>, Constantine J. Athanitis<sup>1</sup>, Emily Been<sup>1</sup>, Peter Ercius<sup>3</sup>, Haiyan Mao<sup>4</sup>, Sirine C. Fakra<sup>6</sup>, Chengyu Song<sup>3</sup>, Ryan C. Davis<sup>7</sup>, Jeffrey A. Reimer<sup>4</sup>, John Vinson<sup>5</sup>, Michal Bajdich<sup>2\*</sup>, Yi Cui<sup>1,8\*</sup>

<sup>1</sup>*Department of Material Science and Engineering, Stanford University, Stanford California, USA.*

<sup>2</sup>*SUNCAT Center for Interface Science and Catalysis, SLAC National Accelerator Laboratory, 2575 Sand Hill Road, Menlo Park, California, USA.*

<sup>3</sup>*The Molecular Foundry, Lawrence Berkeley National Laboratory, Berkeley, California, USA.*

<sup>4</sup>*Department of Chemical and Biomolecular Engineering, University of California, Berkeley, California, USA.*

<sup>5</sup>*Material Measurement Laboratory, National Institute of Standards and Technology, Gaithersburg, Maryland, USA.*

<sup>6</sup>*Advanced Light Source, Lawrence Berkeley National Laboratory, Berkeley, California, USA.*

<sup>7</sup>*Stanford Synchrotron Radiation Light source, SLAC National Accelerator Laboratory, 2575 Sand Hill Road, Menlo Park, California, USA.*

<sup>8</sup>*Stanford Institute for Materials and Energy Sciences, SLAC National Accelerator Laboratory, Menlo Park, California, USA.*

<sup>†</sup>They contributed equally to this work.

\*Correspondence and requests for materials should be addressed to Y.C. (yicui@stanford.edu) or M.B. (bajdich@slac.stanford.edu)

The efficiency of the synthesis of renewable fuels and feedstocks from electrical sources is limited at present by the sluggish water oxidation reaction. Single atom catalysts (SACs) with a controllable coordination environment and exceptional atom utilization efficiency open new paradigms towards designing high performance water oxidation catalysts. Here, using *operando* X-ray absorption spectroscopy measurements with calculations of spectra and electrochemical activity, we demonstrate that the origin of water oxidation activity of IrNiFe SACs is the presence of highly oxidized Ir single atom ( $\text{Ir}^{5.3+}$ ) in the NiFe oxyhydroxide under operating conditions. We show that the optimal water oxidation catalyst could be achieved by systematically increasing the oxidation state and modulating the coordination environments of the Ir active sites anchored atop the NiFe oxyhydroxide layers. Based on the proposed mechanism, we have successfully anchored Ir single-atom sites on NiFe oxyhydroxides ( $\text{Ir}_{0.1}/\text{Ni}_9\text{Fe}$  SAC) via a unique *in situ* cryogenic photochemical reduction (*in situ* Cryo-PCR) method which delivers an overpotential of 183 millivolts at 10 milliamperes per square centimeter and retains its performance following 20 hours of operation in 1 M KOH electrolyte, outperforming the reported catalysts and the commercial  $\text{IrO}_2$  catalysts. These findings open the avenue towards atomic-level understanding of oxygen evolution of catalytic centers under *in operando* condition.

**One-sentence summary aimed at non-specialist readers:** The origin of water oxidation activity in an Ir single atom catalyst is revealed experimentally and theoretically.

54 Efficient and cost-effective electrocatalysts play critical roles in energy conversion and storage and  
55 the societal pursuit of sustainable energy (1-3). The water oxidation reaction, also known as oxygen  
56 evolution reaction (OER), in particular is an enabling process for diverse clean energy technologies  
57 including water splitting (4-6), solar fuels (2), CO<sub>2</sub> reduction (7), and rechargeable metal-air  
58 batteries (8). Unfortunately, the kinetics of the OER are sluggish, which limits the power conversion  
59 efficiency and the overall efficiency.

60 Very recently, higher valence transition metal ions such as Co<sup>4+</sup> (9-11), Ni<sup>4+</sup> (12-14), and Fe<sup>4+/5+</sup>  
61 (15, 16) generated through a potential-dependent deprotonation reaction have been incorporated  
62 into metal oxides/hydroxides resulting in enhanced water oxidation activity. Incorporating precious  
63 metals such as Ir, Ru, and Pt is much less explored, but they offer greater opportunities due to their  
64 tendency towards forming single-atom sites. Computational work has predicted either direct  
65 substitution of Ni<sup>4+</sup> and Fe<sup>4+</sup> by Ir<sup>4+</sup> and Ru<sup>4+</sup>, or that the metal would be close to its most stable +4  
66 oxidation state based on the high stability of the rutile phase (17-20). On the other hand, the high  
67 activity of Sr-leached SrIrO<sub>3</sub>/IrO<sub>x</sub> and Li-removed Li<sub>x</sub>IrO<sub>3</sub> catalysts (5, 21, 22), and a recent  
68 prediction of highly active and high-oxidation homogeneous water oxidation systems (23) indicate  
69 that increased oxidation may lead to improved activity if the active site can be stabilized under  
70 operating conditions.

71 Single-atom catalysts (SACs) have offered an ideal system to precisely control the local  
72 coordination environments and oxidation states of the single site centers (24-29). The single-atom  
73 nature of these active centers leads to a well-defined coordination environments and enhanced  
74 metal-support interactions, which provide remarkable catalytic performance in a number of  
75 heterogeneous reactions, including in the water-gas shift reaction (24), heterogeneous reduction of  
76 CO<sub>2</sub> processes (27), CO oxidation (28), and oxygen reduction reaction (29). We adopted this  
77 strategy and sought to incorporate high-oxidation Ir metal sites into the support to enhance the water  
78 oxidation activity.

79 Here we developed a new *in situ* cryogenic photochemical reduction method (*in situ* Cryo-PCR)  
80 for anchoring Ir single sites on the NiFe oxyhydroxide support for the first time. Density functional  
81 theory (DFT) calculations predict unusually stable IrO<sub>6</sub> octahedral SAC anchored atop the NiFe  
82 oxyhydroxide layers. *In operando* Ir L<sub>3</sub>-edge X-ray absorption spectroscopy combined with spectra  
83 simulations of Ir L<sub>3</sub>-edge of such structures revealed high oxidation of Ir (+5.3) in the NiFe  
84 oxyhydroxides under operating conditions, in agreement with DFT predictions and spectra  
85 calculations. The highly oxidized Ir single site exhibits exceptional OER performance, with a 183  
86 millivolts overpotential at 10 milliamperes per square centimeter, outperforming the precious metal  
87 oxide IrO<sub>2</sub>. These findings are further corroborated by our calculations of the theoretical OER  
88 overpotentials which show that increasing the Ir oxidation state leads to improved activity, and an  
89 overpotential of 0.184 V is obtained for the most oxidized NiFeIr:3O SAC. Such structural and  
90 compositional heterogeneity poses a key obstacle to unambiguously identifying the exact atomistic  
91 structure of the active sites and to further establishing a definitive correlation with the catalytic  
92 properties that can guide the subsequent design of future generations of SACs.

## 93 **Results and Discussions**

94 **Ir single sites on NiFe oxyhydroxides.** In order to test our hypothesis, we set out to explore how  
95 Ir is incorporated into NiFe oxyhydroxides. Using DFT, we have compared the free energy of Ir  
96 substituting either Ni or Fe within the NiFeOOH layered structure (NiFe) to the free energy of  
97 anchoring oxidized Ir atop of the NiFe layer (**Fig. 1A**). For NiFe, we used a widely adopted  $\gamma$ -  
98 NiFeOOH bulk model with interlaced and solvated K<sup>+</sup> cations and protons, since 1 M KOH was  
99 used as electrolyte in the experiment (See SI for Computational Details) (18, 30, 31). Out of a large  
100 number of tested cases, only two possibilities had significant negative free energy of Ir doping (**Fig.**  
101 **1A** and **Fig. S1**). The two stable configurations are 1) a conventional in-layer substitutional doping  
102 of Ir<sup>4+</sup> replacing Ni<sup>4+</sup> (NiFeIr) (17, 18) and 2) single IrO<sub>6</sub> octahedron bonded directly to the NiFe  
103 layer, which we refer to as the single atom catalyst (NiFeIr SAC) configuration. A similar Ir SAC

104 configuration was recently proposed by Zhao et al. utilizing a  $\text{Fe}_2\text{O}_3$  support (32). The protonation  
105 of the three outermost oxygens and the resulting Ir high oxidation state in the NiFeIr SAC is a direct  
106 function of applied voltage (SAC NiFeIr:3OH vs. NiFeIr:3O), but its stability is always greater than  
107 that of NiFeIr ( $> 28 \text{ kJ/mol}$ ) (**Fig. 1A** and **Fig. S1**). The remarkable ability of Ir to sustain a high  
108 oxidation state, the availability to form multiple oxygen bonds at the NiFe layer, and the  
109 stabilization by nearby solvent allow for the presence of such a stable SAC configuration.

110 In light of the theoretical prediction, we sought to synthesize Ir single atoms on NiFe oxyhydroxides  
111 ( $\text{Ir}_{0.1}/\text{Ni}_9\text{Fe}$  SAC) via the *in situ* cryogenic-photochemical reduction method (**Fig. 1B**). In this  
112 method, we first synthesized highly nanoporous  $\text{Ni}_9\text{Fe}$  oxyhydroxides as the support (6). Scanning  
113 electron microscopy image of  $\text{Ni}_9\text{FeOOH}$  substrates showed nanoporous morphology of  
114  $\text{Ni}_9\text{FeOOH}$  (**Fig. S2**). X-ray photoelectron spectroscopy (XPS) of Ni 2p  $\text{Ni}_9\text{FeOOH}$  substrates (**Fig.**  
115 **S3**). The core-level Ni 2p XPS spectra indicate that Ni is in  $\text{Ni}^{2+}$  oxidation state, exhibiting two  
116 peaks at 855.7 eV and 873.3 eV, respectively. The Fe 2p XPS spectra show that Fe is in an oxidation  
117 state of  $\text{Fe}^{3+}$ . Next, a mixed aqueous solution of  $\text{IrCl}_3(\text{H}_2\text{O})_3$  and  $\text{Ni}_9\text{Fe}$  oxyhydroxides was frozen  
118 quickly in liquid nitrogen ( $-196.5 \text{ }^\circ\text{C}$ ) to form a thin layer of ice. Then, the frozen solution was  
119 exposed to UV irradiation on a cooling stage with a temperature of  $-35 \text{ }^\circ\text{C}$  for 1 h. After the UV  
120 treatment, the frozen solution was kept for 24 hours in dark conditions at  $4 \text{ }^\circ\text{C}$ . After centrifuging,  
121 washing, and freezing-drying the samples multiple times, the samples from the *in situ* cryogenic-  
122 photochemical process were stabilized on  $\text{Ni}_9\text{Fe}$  oxyhydroxide supports (see also Supplementary  
123 Information). Aberration corrected high-angle annular dark field-scanning transmission electron  
124 microscopy (HAADF-STEM) showed Ir dispersed on  $\text{Ni}_9\text{Fe}$  oxyhydroxides as individual atoms  
125 (**Fig. 1C**). From inductively coupled plasma optical emission spectrometry (ICP-OES) analysis, we  
126 determined the molar ratio of Ni:Fe:Ir to be 9:1:0.1. Clusters were formed when increasing the Ir  
127 loading on  $\text{Ni}_9\text{FeOOH}$  supports (**Fig. S4**). Using the theoretical prediction and new *in situ*

128 cryogenic-photochemical synthesis, we have achieved stabilized and well distributed Ir single atom  
129 sites in the NiFe oxyhydroxides.

130 **The local coordination and electronic structure of Ir<sub>0.1</sub>/Ni<sub>9</sub>Fe SAC.** To investigate the local  
131 electronic configuration and atomic structures of the Ir<sub>0.1</sub>/Ni<sub>9</sub>Fe under OER operating conditions,  
132 we employed an *in situ* electrochemical cell for X-ray absorption spectroscopy (XAS)  
133 measurements combined with absorption spectra simulations and EXAFS fitting (**Fig. 2**). In the  
134 homemade cell (**Fig. S5**), electrochemistry was performed using catalysts on carbon paper as a  
135 working electrode, a Ag/AgCl reference electrode, a platinum wire counter electrode, and 1 M KOH  
136 solution as the electrolyte.

137 The white lines of Ir *L*<sub>3</sub>-edge X-ray absorption near edge structure (XANES) spectra were compared  
138 with the standard Ir foil and commercial IrO<sub>2</sub> for NiFeIr SAC under different applied potentials  
139 (**Fig. 2A**). The energy shift was used to get an estimation of the Ir valence states for each condition.  
140 For Ir<sub>0.1</sub>/Ni<sub>9</sub>Fe SAC at open circuit, the energy position of the white line is very close to that of IrO<sub>2</sub>  
141 reference, indicating a state close to Ir<sup>4+</sup>. When the applied potential was raised to 1.35 V vs. the  
142 reversible hydrogen electrode (RHE), the white line (WL) gradually shifted towards higher  
143 energies, in agreement with the previous IrO<sub>x</sub>/RuO<sub>2</sub> system (33). Using the energy position of Ir  
144 and IrO<sub>2</sub> as references and interpolating the rest of the samples to a linear dependence energy  
145 position versus valence (34), the XAS spectra indicated an Ir valence of +4 for Ir<sub>0.1</sub>/Ni<sub>9</sub>Fe SAC at  
146 open circuit voltage (OCV) and +5.3 for Ir<sub>0.1</sub>/Ni<sub>9</sub>Fe SAC at 1.45 V vs. RHE, respectively (**Fig. 2B**).  
147 The position of the *L*<sub>3</sub> white line shifts to higher energy is in agreement with the expected electronic  
148 state: 5*d*<sup>5</sup> (Ir<sup>4+</sup>) for IrO<sub>2</sub> and Ir<sub>0.1</sub>/Ni<sub>9</sub>Fe SAC at OCV, 5*d*<sup>3.7</sup> (Ir<sup>5.3+</sup>) for Ir<sub>0.1</sub>/Ni<sub>9</sub>Fe SAC at 1.45 V vs.  
149 RHE.

150 The OCEAN code (35, 36) simulation of the XANES region of the Ir *L*<sub>3</sub>-edge (**Fig. 2C**, see also SI  
151 for details) on DFT optimized structures introduced above is in very good agreement with the  
152 experimental data (**Fig. 2A and Fig. S6**). The increase in the WL intensity from IrO<sub>2</sub> to the

calculated NiFeIr, NiFeIr SAC structures in the simulated data implies an increase in oxidation state of the Ir atoms that well matches the experimental trend (**Fig. 2C**). This correlation is further supported when comparing the WL intensity of the calculated spectra vs. DFT Bader charge (**Fig. 2B**). Particularly, the WL intensity obtained experimentally for Ir<sub>0.1</sub>/Ni<sub>9</sub>Fe SAC under operating conditions is consistent with the simulated spectrum of NiFeIr:3OH SAC (**Fig. 2C**) and lies generally in between NiFeIr:3OH and NiFeIr:3O SAC (**Fig. S7**), proving that Ir is present in the high oxidation state under applied bias. Conversely, when the Ir atom substitutes one of the surface Ni atoms (NiFeIr), the Ir oxidation state is much closer to that of IrO<sub>2</sub> as evidenced by a peak height (**Fig. 2C**) and the decrease in white line intensity in the simulated spectrum (**Fig. 2B**). However, the maximum theoretical oxidation state is not reached in the experiment, which is indicative of possible mixture of the NiFeIr SAC and NiFeIr type coordination in the of Ir<sub>0.1</sub>/Ni<sub>9</sub>Fe SAC sample. To further verify that Ir<sub>0.1</sub>/Ni<sub>9</sub>Fe SAC contains only atomically dispersed individual Ir atoms, *in situ* extended X-ray absorption fine structure (EXAFS) spectra were obtained for NiFeIr SAC at open circuit and at operating conditions (**Fig. 2D**). The Ir-Ir contribution at about 2.3 Å is absent in the k<sup>3</sup>-weighted EXAFS at the Ir *L*<sub>3</sub>-edge for both NiFeIr SAC at open circuit and at 1.4 V vs. RHE, strongly indicating that Ir exists as isolated atoms during operating conditions. The only prominent shell located in between 1.5 Å and 2 Å for Ir<sub>0.1</sub>/Ni<sub>9</sub>Fe SAC at open circuit and at 1.4 V vs. RHE, respectively originated from the Ir-O contribution.

**Evaluation of water oxidation activity of Ir<sub>0.1</sub>/Ni<sub>9</sub>Fe SAC.** Next, we explored the water oxidation activity of Ir<sub>0.1</sub>/Ni<sub>9</sub>Fe SAC and relevant controls on Ni foam in 1 M KOH electrolyte. The backward sweep was taken for the calculation of overpotential to avoid any non-faradaic contribution to the total current. Although NiFe oxyhydroxides are indeed the best non-precious metal electrocatalysts, further modification is needed to achieve better performance. Beneficial role of Au on NiFe LDH has been reported recently (37). The Ir<sub>0.1</sub>/Ni<sub>9</sub>Fe SAC achieved the optimal water oxidation catalytic activity with the low overpotential of 183 mV at 10 mA/cm<sup>2</sup> (**Fig. 3A**), superior to that of the best

commercial  $\text{IrO}_2$  ( $\sim 280$  mV) (see also **Table S1** for detailed comparisons). The activity of  $\text{Ir}_{0.1}/\text{Ni}_9\text{Fe}$  SAC is superior to that of the  $\text{Ir}_{0.01}/\text{Ni}_9\text{Fe}$  owing to the formation of more Ir active sites (**Fig. 3A** and **Fig. 3B**). However, upon incorporating higher Ir loading to 10%, the activity of  $\text{Ir}_1/\text{Ni}_9\text{Fe}$  catalyst decreased due to the formation of Ir clusters (**Fig. S4**). The  $\text{Ir}_{0.1}/\text{Ni}_9\text{Fe}$  SAC has the least Tafel slope of 49 mV/dec implying more favourable reaction kinetics toward water oxidation reaction than the control samples (38) (**Fig. 3B**). The electrochemical stability of the  $\text{Ir}_{0.1}/\text{Ni}_9\text{Fe}$  SAC was tested at a constant overpotential of 200 mV on Ni foam for 20 hours (**Fig. 3C**). We observed no appreciable decrease in current density in this time interval.

Lastly, we investigated whether the water oxidation activity of  $\text{Ir}_{0.1}/\text{Ni}_9\text{Fe}$  SAC originates from intrinsic catalytic activity of Ir active sites or exclusively from an enhanced surface area. We analyzed the electrochemically active surface area (ECSA) and ECSA normalized current density at 1.45 V vs. RHE for  $\text{Ir}_{0.1}/\text{Ni}_9\text{Fe}$  SAC and  $\text{Ni}_9\text{FeOOH}$  control (**Fig. 3D**). Based on ECSA results, the intrinsic activity of  $\text{Ir}_{0.1}/\text{Ni}_9\text{Fe}$  SAC is higher than that of  $\text{Ni}_9\text{FeOOH}$  control.  $\text{Ir}_{0.1}/\text{Ni}_9\text{Fe}$  SAC shows the advantages not only in improving OER activity and stability, but also lowering Ir usage and the cost.

**Theoretical activities of NiFeIr water oxidation catalysts.** To complete our analysis of  $\text{Ir}_{0.1}/\text{Ni}_9\text{Fe}$  SAC system, we evaluated theoretical OER overpotentials (see Computational Details in SI) of the obtained stable systems utilizing Ir at edge-sites, subsurface and as single-atom near Fe-sites (adapted from Au single-atom study (37)) in the (100) surface of NiFe labelled as NiFeIr, and octahedral NiFeIr SAC anchored at the NiFe basal planes [(001) facet]. These are compared to (110) surface of rutile  $\text{IrO}_2$  and to Fe-site in NiFe (100) surface obtained previously (31). First, we show that the calculated  $\Delta G_{\text{OOH}}$  to  $\Delta G_{\text{OH}}$  scaling (**Fig. 4A**) for Ir-sites is generally improved over the universal scaling, where  $\text{OOH}^*$  is stabilized with nearby surface oxygens, and is also necessary in order to obtain theoretical overpotentials lower than 0.3 V. Additionally, the sites with Ir in higher oxidation state bind the adsorbates progressively which further increases the  $\text{OOH}^*$



203 stabilization. Theoretically, adding Ir into NiFe oxyhydroxides significantly improves the second  
 204 step ( $\text{OH}^*$  to  $\text{O}^*$ ) in OER mechanism for Ir sites (**Fig. 4B** and **Fig. S9**). The theoretical OER  
 205 overpotentials, shown as a two-dimensional OER volcano plot are summarized in **Figure 4B**.  
 206 The 2D volcano plot further shows that the Ir-site in the  $\text{IrO}_2(110)$  binds significantly stronger  
 207 ( $\Delta G_{\text{OH}}$  is the most negative in **Fig. 4A, B**) than any other model considered and appears in the  
 208 lower-left part of the 2D plot. On the other hand, Fe-site in the NiFe (100) binds significantly  
 209 weaker due to the presence the Fe-O oxo intermediate ( $\Delta G_{\text{OH}}$  is the most positive in **Fig. 4A, B**)  
 210 and appears in the upper-right part of the 2D plot. Additionally, we have tested the effect captured  
 211 by Zhang et.al. for Au/NiFe LDHs on Fe sites (37). Our expanded calculations (**Fig. S9**) show that  
 212 the effect of adding Ir is different that of adding Au in  $\text{Ni}_9\text{FeOOH}$ . Adding single-atom Ir next to  
 213 Fe-active site (**Fig. S9**, structure (i)) results in very reactive  $\text{O}^*$  at the Ir-O-Fe bridge, which leads  
 214 to unfavourable  $\text{O}^*$  to  $\text{OOH}^*$  OER step with overpotential of 1.8 V. For completeness, we have  
 215 also tested the effect of subsurface doping by Ir next to the Fe active site (**Fig. S9**, structure (h)). In  
 216 all tested cases, adding Ir next to Fe did not improve the activity of Fe active site indicating no  
 217 synergetic interaction of Ir on Fe-sites in the NiFe oxyhydroxides. Interestingly, all Ir-sites in the  
 218 NiFeIr and NiFeIr SAC models straddle two extrema set by two structures (**Fig. 4D** and **4E**) in a  
 219 nearly linear fashion. This trend is well correlated with the formal and calculated oxidation states  
 220 the Ir-sites in the NiFeIr (+4.4) and NiFeIr SAC (+4.8 and +5.6) models (**Fig. 2B**). Improved OH-  
 221 OOH scaling and a gradual decrease of  $5d$ -electrons at the Ir-atoms to bond with active oxygen  $2p$ -  
 222 states - indicative of weaker adsorbate bonding - in turn shifts the position of the NiFeIr SAC model  
 223 inside the optimal OER region. A similar system on Ir anchored NiFe oxyhydroxides was developed  
 224 where they discovered that the isolated Ir sites undergo a deprotonation process to form the multiple  
 225  $\text{Ir}^{+3.57}$  active sites during OER, promoting the O-O coupling (39). The final calculated theoretical  
 226 overpotentials are 0.184 V for NiFeIr:3O SAC (**Fig. 4G**), 0.333 V for Ir-site in the NiFeIr(100)  
 227 (**Fig. 4F**), 0.381 V for the Fe-site in NiFe(100) (**Fig. 4E**) and finally, 0.664 V for  $\text{IrO}_2(110)$  (**Fig.**

4D). The very-low overpotential of 0.184 V for NiFeIr SAC is obtained only for well-stabilized OOH intermediate and agrees well with the experimental overpotential of 183 mV for Ir<sub>0.1</sub>/Ni<sub>9</sub>Fe SAC catalyst. A detailed list of DFT energies and structures is provided via the Catalysis-hub.org repository (40, 41).

## Conclusions

In summary, we established a protocol where Ir single-atom sites are stabilized on NiFe oxyhydroxides via a new *in situ* cryogenic photochemical reduction method, which leads to Ir<sub>0.1</sub>/Ni<sub>9</sub>Fe SAC catalysts with superior water oxidation performance. By combining XAS analyses with simulated spectra and calculated OER activity, we unambiguously identify that Ir species adopt a single-atom configuration in an oxidation state greater than +5. The Ir<sub>0.1</sub>/Ni<sub>9</sub>Fe SAC delivers an overpotential of 183 mV at 10 mA cm<sup>-2</sup>, which halves the 0.3-0.4 V OER overpotential wall, and is the best performing Ir-based catalyst known to date. Above experimental findings are further corroborated by the DFT calculations which show that the improved activity is due to weaker binding and improved OH-OOH scaling of the highly oxidized Ir-SAC sites and not a consequence of modification of electronic structure of surface Ni/Fe sites. Importantly, the utilization of NiFe oxyhydroxides as catalytic supports provides an ideal model system to probe and quantitatively establish the correlation between the atomistic structure of the single-metal centers and their catalytic properties for diverse set of electrocatalytic reactions. Our findings demonstrate unique electrochemical properties of single atom catalysts, with general implications for the design of materials employing oxygen redox chemistry.

## Materials and Methods

**Preparation of Ir single atoms /NiFe via *in situ* Cryo-PCR.** Our general *in situ* cryogenic-photochemical reduction synthesis of Ir single atoms /Ni<sub>9</sub>FeOOH is illustrated in **Fig. 1B**. First, a controlled ratio of 0.1 mg ml<sup>-1</sup> IrCl<sub>3</sub>(H<sub>2</sub>O)<sub>3</sub> and Ni<sub>9</sub>FeOOH in aqueous solution in a flat beaker were

253 prepared in a beaker and the beaker is frozen quickly in liquid nitrogen (-196.5 °C) bath in dark  
254 conditions, keeping the beaker flat. The mixed solution can be frozen quickly to form ultrathin ice,  
255 which ensures the homogeneous distribution of Ir precursor molecules in solution can be  
256 maintained during solidification process. Second, the frozen ice was exposed to UV irradiation on  
257 a cooling stage with a temperature of -35 °C for 1 h in an environmental chamber (Associated  
258 Environmental Systems, Acton, MA), avoiding ice melting and forming Ir single atoms on  
259 Ni<sub>9</sub>FeOOH support. The powder density of the UV light near ice was measured (0.7 mW cm<sup>-2</sup>)  
260 using a radiometer (Newport Model PMKIT-05-01). Then, the Ir single atoms on Ni<sub>9</sub>FeOOH  
261 samples were filtered, cleaned and dried in vacuo in a Labconco FreeZone 6 freeze dryer. Finally,  
262 the Ir<sub>0.1</sub>/Ni<sub>9</sub>Fe SACs were collected.

263 **Characterization.** High-angle annular dark-field scanning transmission electron microscopy  
264 (HAADF-STEM) were taken on a TEAM 0.5 transmission electron microscope operated at 300 kV  
265 at National Center for Electron Microscopy (NCEM). The samples were prepared by dropping  
266 catalyst powder dispersed in ethanol onto carbon-coated copper TEM grids (Ted Pella, Redding,  
267 CA) using micropipettes and were dried under ambient conditions. The atomic composition of  
268 Ir/NiFe catalysts was determined using an Inductively Coupled Plasma Optical Emission  
269 Spectrometer (ICP-OES Agilent Dual-View 720 with CCD for full wavelength coverage between  
270 167 to 785 nm.).

271 **In situ X-ray absorption.** In the homemade cell, electrochemistry was performed using catalysts  
272 on carbon paper as a working electrode, a Ag/AgCl reference electrode, a platinum wire counter  
273 electrode, and 1 M KOH solution as the electrolyte (**Fig. S5**). The *in situ* Ir L<sub>3</sub>-edge XAS data were  
274 collected at X-Ray Fluorescence Microprobe (XFM) beamline 10.3.2 at the Advanced Light Source  
275 (ALS) and beamline 4-1 at the Stanford Synchrotron Radiation Lightsource (SSRL). The ALS data  
276 were pre-processed (deadtime corrected, calibrated and deglitched) using custom LabVIEW  
277 software available at the beamline. We used Athena software to calibrate the energy scale, to correct

the background signal and to normalize the intensity. The spectra were normalized with respect to the edge height after subtracting the pre-edge and post-edge backgrounds using Athena software. To extract EXAFS oscillations, background was removed in k-space using a five-domain cubic spline. The resulting k-space data,  $k^3\chi(k)$ , was then Fourier transformed. Ir  $L_3$ -edge EXAFS were fitted in R-space with the DFT optimized NiFeIr:3Os model (**Fig. S8**).

**Electrochemical Measurements.** Electrochemical measurements were performed using a three-electrode system connected to an electrochemical workstation (Bio-Logic VMP3) with built-in electrochemical impedance spectroscopy (EIS) analyzer. The working electrode was catalysts deposited on Ni foam. Ag/AgCl (with saturated KCl as the filling solution) and platinum foil were used as reference and counter electrodes, respectively. To load the catalyst on a Ni foam, 20 mg of catalyst was dispersed in a mixture containing 2 ml of water and 2 ml ethanol, followed by the addition of 100  $\mu$ L Nafion solution. The suspension was sonicated for 30 min to prepare a homogeneous ink. Ni foam coated with water resistant silicone glue was drop-casted with the catalyst ink. Unless otherwise stated, all experiments were performed at ambient temperature ( $22 \pm 2$  °C) and electrode potentials were converted to the RHE scale using  $E(\text{RHE}) = E(\text{Ag/AgCl}) + 0.197 \text{ V} + 0.059 \cdot \text{pH}$ .

Electrochemical surface area measurement (ECSA) of each catalyst was calculated based on measuring their electrochemical capacitances. We measured the CVs in a narrow non-Faradaic potential window in which the change of the current is principally due to the charging of the double-layer, which is expected to be linearly proportional to the active surface area. The measured capacitive current densities at the average potential in the selected range were plotted as a function of scan rates and the slope of the linear fit was calculated as the double-layer capacitance ( $C_{dl}$ ). The ECSA of the catalyst is calculated from the following equation,

$$\text{ECSA} = C_{dl} / C_s$$

302 Cs is the specific capacitance in 1 M KOH electrolytes. The intrinsic activity was obtained by  
 303 normalizing the current to the ECSA to exclude the effect of surface area on catalytic performance.

304 **DFT calculations of bulk and surface models.** The density functional calculations were  
 305 performed within the Vienna ab initio simulation package (VASP) using the projector augmented  
 306 wave (PAW) potentials. We employed the PBE functional together with the Hubbard-*U* correction  
 307 method applied for the *d*-electrons of Ni ( $U-J=U_{\text{eff}} = 6.45$  eV) and Fe ( $U_{\text{eff}} = 4.3$  eV) atoms. For Ni,  
 308 the  $U_{\text{eff}}$  parameter is chosen according to the Materials Project Database, while for Fe, it was taken  
 309 from recent NiFeOOH paper of Martirez and Carter. For NiFeOOH system, other authors have used  
 310 similar values for NiFeOOH that are within +/- 1 eV. The bulk optimization calculations were  
 311 performed at the energy cutoff of 600 eV on the  $3 \times 3 \times 4$  *k*-point mesh per  $3 \times 3 \times 2$  unit cell of  
 312 the  $\gamma$ -NiFeOOH ( $\text{K}_8(\text{Ni}_{22}\text{Fe}_2)\text{O}_{48} + 16\text{H}_2\text{O}$ ) used in our recent work. In this cell, single Ir atom was  
 313 placed either in the conventional in-layer substitutional doping (replacing  $\text{Ni}^{4+}$ ,  $\text{Ni}^{3+}$  and  $\text{Fe}^{4+}$  sites)  
 314 or in the SAC configuration with relative to Ni and Fe and variable OH\*/O\* groups (see results of  
 315 **Fig. S1**).

316 For surfaces, we have employed  $3 \times 1$  symmetric (100) slabs of four layers of M–O (keeping bottom  
 317 two fixed) and  $3 \times 2 \times 2$  (001) basal plane (bottom layer fixed) and 15 Å of a vacuum. Here we  
 318 used 500 eV energy cutoff and the  $4 \times 4 \times 1$  and  $(3 \times 3 \times 1)$  *k*-point meshes, respectively. Full  
 319 relaxation below a minimum threshold force of  $0.02 \text{ eV}/\text{\AA}^2$  was performed in all cases. Finally, to  
 320 obtain the theoretical overpotential for each surface, the standard OER mechanism and which has  
 321 been applied to many types of oxides ( $* \rightarrow \text{OH}^*$ ,  $\text{OH}^* \rightarrow \text{O}^*$ ,  $\text{O}^* \rightarrow \text{OOH}^*$ ,  $\text{OOH}^* \rightarrow \text{O}_2(\text{g})$ ) was  
 322 assumed. The Gibbs free energies of the OER intermediates calculated via computational hydrogen  
 323 electrode method include room temperature corrections, zero point energy (ZPE), and the  
 324 vibrational enthalpy and entropy contributions (relative to  $\text{H}_2(\text{g})$  and  $\text{H}_2\text{O}(\text{l})$ ) obtained by means of  
 325 the harmonic approximation. Combined effect of total energies of adsorption is:  $\Delta G_{\text{corr.}}(\text{OH}^*) =$   
 326  $0.302 \text{ eV}$ ,  $\Delta G_{\text{corr.}}(\text{O}^*) = -0.015 \text{ eV}$ , and  $\Delta G_{\text{corr.}}(\text{OOH}^*) = 0.345 \text{ eV}$ , respectively. The fully

327 optimized bulk models, reference structures and their respective energies are included as part of the  
328 Catalysis-hub.org repository.

329 **Computation of the Spectra.** The Ir  $L_3$ -edge for the different structures was calculated using the  
330 OCEAN code. Electron wave functions were generated using the QUANTUMESPRESSO code.  
331 The norm-conservative pseudopotentials for Ir and O generated using the FHI98PP package using  
332 Trouiller-Martins-type, PBE-GGA were utilized. For the simulation of rutile IrO<sub>2</sub> and Ir metal  
333 experimental crystallographic structures were used (ICSD #84577 and #640730, respectively) with  
334 a k-points sampling of (4x4x4), 1000 screening bands and (2x2x2) k-points sampling for the  
335 screening calculation. For the DFT generated structures, the k-points sampling was decreased to  
336 (2x2x1) with 2000 screening bands. The same core-offset energy, plane-wave energy cut-off (120  
337 Rydberg) and broadening (3.5 eV) were utilized for all the simulations.

338 The simulated spectra were normalized and aligned to the experimental results. The WL (white  
339 line) was numerically integrated after fitting the data using Lorentzian and arctangent fit function  
340 (**Fig. S6**). The WL intensity was normalized by the WL intensity of the simulation for rutile IrO<sub>2</sub>.  
341 The WLs of the experimental data were normalized in the same way using the experimental IrO<sub>2</sub>  
342 as standard.

### 343 **Data availability**

344 All the data supporting the findings of this study are available within the paper and its  
345 Supplementary Materials or from the corresponding author on request.

### 346 347 **Acknowledgements**

348  
349 This work was supported by the Department of Energy (DOE), Office of Basic Energy Sciences,  
350 Division of Materials Sciences and Engineering (contract no. DE-AC02-76SF00515) and by DE-  
351 SC0008685 to the SUNCAT Center of Interface Science and Catalysis. *The Advanced Light Source*  
352 and Molecular Foundry are supported by the Director, Office of Science, Office of Basic Energy

353 Sciences, of the U.S. Department of Energy under Contract No. DE-AC02-05CH11231 and the use  
354 of the computer time allocation for the “Transition metal-oxide and metal surfaces: applications  
355 and reactivity trends in catalysis” at the National Energy Research Scientific Computing Center, a  
356 DOE Office of Science User Facility supported by the Office of Science of the U.S. Department of  
357 Energy under Contract No. DE-AC02-05CH11231. Use of the Stanford Synchrotron Radiation  
358 Light Source, SLAC National Accelerator Laboratory, is supported by the U.S. Department of  
359 Energy, Office of Science, Office of Basic Energy Sciences under Contract No. DE-AC02-  
360 76SF00515. We acknowledge the support on electron microscopy from Stanford Nano Shared  
361 Facilities.

362 **Author contributions**

363 Y.C. supervised all aspects of the work and M.B designed the theoretical study. Y.C., X.Z. and J.T.  
364 conceived the idea. X.Z. and J.T. designed the research, performed the synthesis, most of the  
365 structural characterizations and electrochemical tests. X.Z., S.F. and R.D. performed in operando  
366 X-ray studies. J.T. developed in situ cryogenic-photochemical reduction (in situ Cryo-PCR)  
367 platform, synthesized cryogenic Iridium Single Atom Catalyst (Cryo-Ir SAC) and did the  
368 magnetron sputtering deposition. X.Z., J.T., P.E, and C.S. contributed transmission electron  
369 microscopy studies. X.Y. and C.J.A helped with experiments. J.A.G.T. and M.B. performed the  
370 theoretical calculations. The calculations of spectra were performed by A.G. and J.V. E.B., H.M.  
371 and J.A.R contributed to helpful and valuable discussions besides solid-state nuclear magnetic  
372 resonance (SS-NMR). The paper was co-written by X.Z, J.T., A. G., M.B. and Y.C. with input from  
373 all authors. All authors discussed the results and commented on the final manuscript.

374 **Additional information**

375 Supplementary information is available online. The computational data is stored in the Catalysis-  
376 hub.org repository (40, 41). Reprints and permissions information is available online at

377 [www.nature.com/reprints](http://www.nature.com/reprints). Correspondence and requests for materials should be addressed to Y.C.  
378 or M.B.

379 **Competing interests**

380 The authors declare no competing interests.

381  
382  
383  
384  
385  
386  
387



- 389 1. P. De Luna *et al.*, What would it take for renewably powered electrosynthesis to displace  
390 petrochemical processes? *Science* **364**, (2019).
- 391 2. H. B. Gray, Powering the planet with solar fuel. *Nature chemistry* **1**, 7 (2009).
- 392 3. Z. W. Seh *et al.*, Combining theory and experiment in electrocatalysis: Insights into  
393 materials design. *Science* **355**, (2017).
- 394 4. T. Wu *et al.*, Iron-facilitated dynamic active-site generation on spinel CoAl<sub>2</sub>O<sub>4</sub> with self-  
395 termination of surface reconstruction for water oxidation. *Nature Catalysis* **2**, 763-772  
396 (2019).
- 397 5. L. C. Seitz, C. F. Dickens, A highly active and stable IrOx/SrIrO<sub>3</sub> catalyst for the oxygen  
398 evolution reaction. *Science* **353**, 1011-1014 (2016).
- 399 6. B. Zhang, X. Zheng, O. Voznyy, Homogeneously dispersed multimetal oxygen-evolving  
400 catalysts. *Science* **352**, 333-337 (2016).
- 401 7. X. Zheng *et al.*, Theory-driven design of high-valence metal sites for water oxidation  
402 confirmed using in situ soft X-ray absorption. *Nature chemistry* **10**, 149-154 (2017).
- 403 8. P. Albertus, S. Babinec, S. Litzelman, A. Newman, Status and challenges in enabling the  
404 lithium metal electrode for high-energy and low-cost rechargeable batteries. *Nature*  
405 *Energy* **3**, 16-21 (2017).
- 406 9. J. Zhou *et al.*, Electrochemically accessing ultrathin Co (oxy)-hydroxide nanosheets and  
407 operando identifying their active phase for the oxygen evolution reaction. *Energy &*  
408 *Environmental Science* **12**, 739-746 (2019).
- 409 10. A. Moysiadou, S. Lee, C. S. Hsu, H. M. Chen, X. Hu, Mechanism of Oxygen Evolution  
410 Catalyzed by Cobalt Oxyhydroxide: Cobalt Superoxide Species as a Key Intermediate and  
411 Dioxygen Release as a Rate-Determining Step. *Journal of the American Chemical Society*  
412 **142**, 11901-11914 (2020).
- 413 11. M. Bajdich, M. García-Mota, A. T. Bell, Theoretical Investigation of the Activity of  
414 Cobalt Oxides for the Electrochemical Oxidation of Water. *Journal of the American*  
415 *Chemical Society*, 13521-13530 (2013).
- 416 12. X. Su *et al.*, Operando Spectroscopic Identification of Active Sites in NiFe Prussian Blue  
417 Analogues as Electrocatalysts: Activation of Oxygen Atoms for Oxygen Evolution  
418 Reaction. *Journal of the American Chemical Society* **140**, 11286-11292 (2018).
- 419 13. M. Gorlin *et al.*, Oxygen Evolution Reaction Dynamics, Faradaic Charge Efficiency, and  
420 the Active Metal Redox States of Ni-Fe Oxide Water Splitting Electrocatalysts. *Journal of*  
421 *the American Chemical Society* **138**, 5603-5614 (2016).
- 422 14. D. K. Bediako *et al.*, Structure-activity correlations in a nickel-borate oxygen evolution  
423 catalyst. *Journal of the American Chemical Society* **134**, 6801-6809 (2012).
- 424 15. J. Y. Chen *et al.*, Operando Analysis of NiFe and Fe Oxyhydroxide Electrocatalysts for  
425 Water Oxidation: Detection of Fe(4+) by Mossbauer Spectroscopy. *Journal of the*  
426 *American Chemical Society* **137**, 15090-15093 (2015).
- 427 16. H. Dau, Water Splitting: Unexpected Fe(VI) Trapped by Manipulation of Reaction  
428 Kinetics. *Chem* **4**, 668-670 (2018).
- 429 17. V. Tripkovic, H. A. Hansen, T. Vegge, From 3D to 2D Co and Ni Oxyhydroxide  
430 Catalysts: Elucidation of the Active Site and Influence of Doping on the Oxygen  
431 Evolution Activity. *ACS Catalysis* **7**, 8558-8571 (2017).
- 432 18. H. Shin, H. Xiao, W. A. Goddard, 3rd, In Silico Discovery of New Dopants for Fe-Doped  
433 Ni Oxyhydroxide (Ni<sub>1-x</sub>Fe<sub>x</sub>OOH) Catalysts for Oxygen Evolution Reaction. *Journal of*  
434 *the American Chemical Society* **140**, 6745-6748 (2018).

19. P. Li *et al.*, Boosting oxygen evolution of single-atomic ruthenium through electronic coupling with cobalt-iron layered double hydroxides. *Nature communications* **10**, 1711 (2019).
20. H. N. Nong *et al.*, A unique oxygen ligand environment facilitates water oxidation in hole-doped IrNiOx core-shell electrocatalysts. *Nature Catalysis* **1**, 841-851 (2018).
21. P. E. Pearce *et al.*, Revealing the Reactivity of the Iridium Trioxide Intermediate for the Oxygen Evolution Reaction in Acidic Media. *Chemistry of Materials* **31**, 5845-5855 (2019).
22. C. Yang *et al.*, Cation insertion to break the activity/stability relationship for highly active oxygen evolution reaction catalyst. *Nature communications* **11**, 1378 (2020).
23. M. J. Craig *et al.*, Universal scaling relations for the rational design of molecular water oxidation catalysts with near-zero overpotential. *Nature communications* **10**, 4993 (2019).
24. S. Yao, X. Zhang, Atomic-layered Au clusters on a-MoC as catalysts for the low-temperature water-gas shift reaction. *Science* **357**, 389-393 (2017).
25. Y. Yao *et al.*, High temperature shockwave stabilized single atoms. *Nat Nanotechnol* **14**, 851-857 (2019).
26. H. Wei *et al.*, Iced photochemical reduction to synthesize atomically dispersed metals by suppressing nanocrystal growth. *Nature communications* **8**, 1490 (2017).
27. X. Shao *et al.*, Iridium Single-Atom Catalyst Performing a Quasi-homogeneous Hydrogenation Transformation of CO<sub>2</sub> to Formate. *Chem* **5**, 693-705 (2019).
28. Y. Lu *et al.*, Identification of the active complex for CO oxidation over single-atom Ir-on-MgAl<sub>2</sub>O<sub>4</sub> catalysts. *Nature Catalysis* **2**, 149-156 (2018).
29. H. Fei *et al.*, General synthesis and definitive structural identification of MN<sub>4</sub>C<sub>4</sub> single-atom catalysts with tunable electrocatalytic activities. *Nature Catalysis* **1**, 63-72 (2018).
30. J. Zaffran *et al.*, Influence of Electrolyte Cations on Ni(Fe)OOH Catalyzed Oxygen Evolution Reaction. *Chemistry of Materials* **29**, 4761-4767 (2017).
31. J. G. Baker *et al.*, The Role of Aluminum in Promoting Ni-Fe-OOH Electrocatalysts for the Oxygen Evolution Reaction. *ACS Applied Energy Materials* **2**, 3488-3499 (2019).
32. Y. Zhao *et al.*, Stable iridium dinuclear heterogeneous catalysts supported on metal-oxide substrate for solar water oxidation. *Proc Natl Acad Sci U S A* **115**, 2902-2907 (2018).
33. A. F. Pedersen *et al.*, Operando XAS Study of the Surface Oxidation State on a Monolayer IrOx on RuOx and Ru Oxide Based Nanoparticles for Oxygen Evolution in Acidic Media. *J Phys Chem B* **122**, 878-887 (2018).
34. J. P. Clancy *et al.*, Spin-orbit coupling in iridium-based 5d compounds probed by x-ray absorption spectroscopy. *Physical Review B* **86**, (2012).
35. J. Vinson, J. J. Rehr, J. J. Kas, E. L. Shirley, Bethe-Salpeter equation calculations of core excitation spectra. *Physical Review B* **83**, (2011).
36. K. Gilmore *et al.*, Efficient implementation of core-excitation Bethe-Salpeter equation calculations. *Computer Physics Communications* **197**, 109-117 (2015).
37. J. Zhang *et al.*, Single-Atom Au/NiFe Layered Double Hydroxide Electrocatalyst: Probing the Origin of Activity for Oxygen Evolution Reaction. *Journal of the American Chemical Society* **140**, 3876-3879 (2018).
38. Y.-H. Fang, Z.-P. Liu, Tafel Kinetics of Electrocatalytic Reactions: From Experiment to First-Principles. *ACS Catalysis* **4**, 4364-4376 (2014).
39. K. Jiang *et al.*, Dynamic active-site generation of atomic iridium stabilized on nanoporous metal phosphides for water oxidation. *Nature communications* **11**, 2701 (2020).
40. K. T. Winther *et al.*, Catalysis-Hub.org, an open electronic structure database for surface reactions. *Sci Data* **6**, 75 (2019).
41. <https://www.catalysis-hub.org/publications/ZhengOrigin2020>.

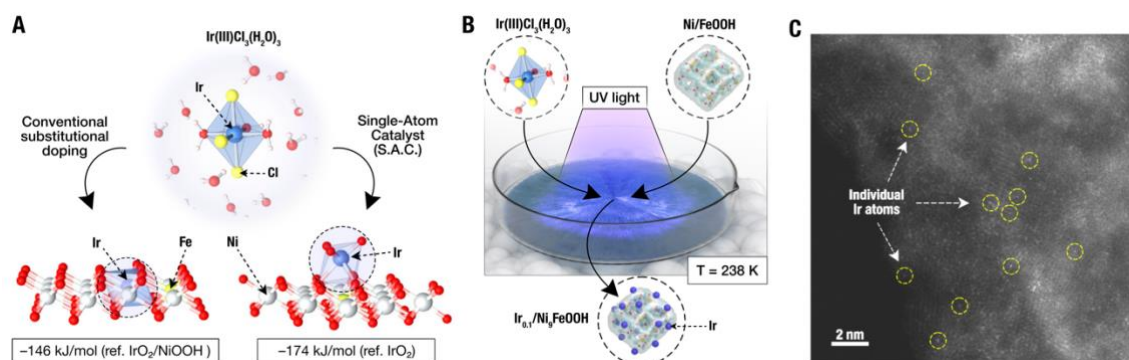


**Fig. 1 | The preparation route to Ir single-atom on NiFe oxyhydroxides and atomic structure characterizations of NiFeIr by HAADF-STEM.** (A) A DFT prediction of a preferred Ir atom embedding within the NiFeOOH layered structure under operating conditions. The conventional in-layer substitution of Ni<sup>4+</sup> by Ir<sup>4+</sup> (NiFeIr) (left) is compared to a more preferred single IrO<sub>6</sub> octahedron bonded to NiFe layer, in SAC configuration (NiFeIr SAC) (right). The energies with respect to given references are at zero bias. Note that NiFeIr SAC maintains its overall stability even under applied voltage (**Fig. S1**). (B) *In situ* cryogenic-photochemical reduction synthesis of Ir<sub>0.1</sub>/Ni<sub>9</sub>Fe samples. (C) HAADF-STEM image of Ir single-atoms on Ni<sub>9</sub>FeOOH supports (Ir<sub>0.1</sub>/Ni<sub>9</sub>Fe). Representative Ir single atoms are shown as bright spots with yellow circles.

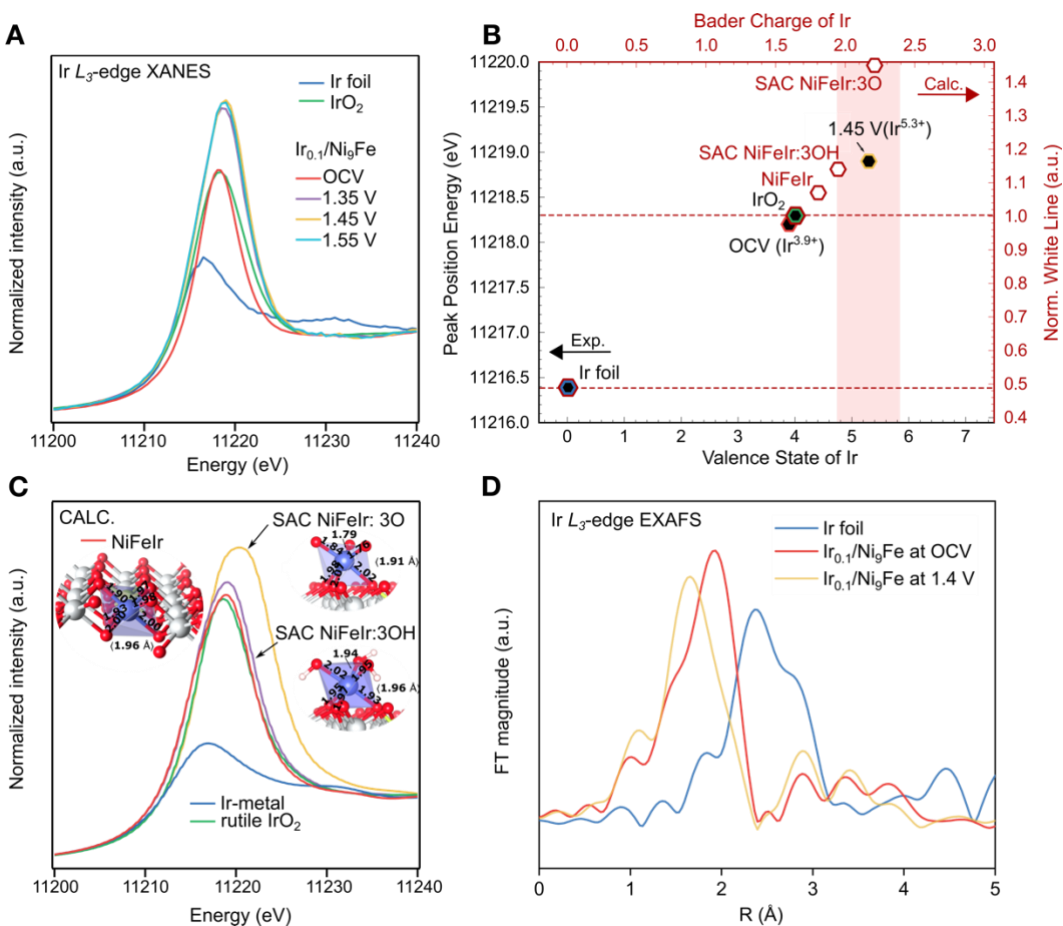


**Fig. 2 | *In operando* XAS characterization of the Ir<sub>0.1</sub>/Ni<sub>9</sub>Fe catalyst coupled to DFT simulated spectra.** (A) Experimental Ir- $L_3$  edge XANES spectra of Ir<sub>0.1</sub>/Ni<sub>9</sub>Fe SAC at OCV and after applying 1.35 V, 1.45 V, and 1.55 V vs. RHE. (B) White line position of Ir<sub>0.1</sub>/Ni<sub>9</sub>Fe SAC during water oxidation reactions. Ir foil and IrO<sub>2</sub> were used as references for the oxidation states of 0 and +4. For comparison, the normalized white line (WL) intensity from DFT simulated spectra is also shown on the separate y-axis. (C) Theoretical Ir  $L_3$ -edge XANES spectra of Ir foil, rutile-IrO<sub>2</sub>, Ir doped sites (NiFeIr) and Ir anchored sites (NiFeIr SAC) (see also **Fig. 1** and **Fig. 4**). Insets show the corresponding differences in the structural models and calculated Bader charges indicating higher oxidation states for SAC structure. (D) Experimental Ir  $L_3$ -edge EXAFS spectra of Ir foil, Ir<sub>0.1</sub>/Ni<sub>9</sub>Fe at OCV, and at 1.4 V vs. RHE.

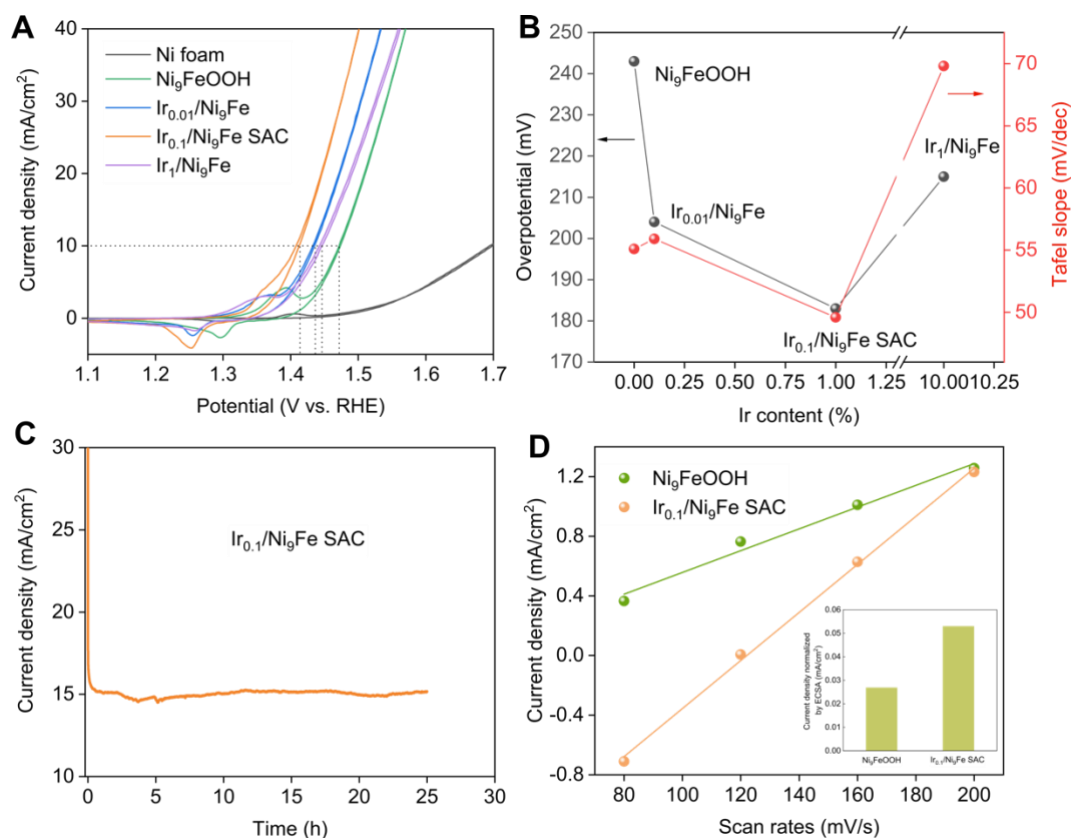


**Fig. 3 | Performance of Ir<sub>0.1</sub>/Ni<sub>9</sub>Fe SAC and controls in the three-electrode system.** (A) The OER polarization curves and (B) Overpotential at 10 mA/cm<sup>2</sup> and Tafel slopes of Ir<sub>0.1</sub>/Ni<sub>9</sub>Fe SAC and controls loaded on Ni foam in 1 M KOH. (C) Chronoamperometry measurement of Ir<sub>0.1</sub>/Ni<sub>9</sub>Fe SAC on Ni foam electrode at a constant potential of 1.43 V vs. RHE for 20 hours. (D) Current density of Ir<sub>0.1</sub>/Ni<sub>9</sub>Fe SAC and Ni<sub>9</sub>FeOOH control plotted versus scan rates. The slopes obtained from a linear fit were used to represent ECSA. The inset showed the ECSA normalized current density at 1.45 V vs. RHE for Ir<sub>0.1</sub>/Ni<sub>9</sub>Fe SAC and Ni<sub>9</sub>FeOOH, respectively.

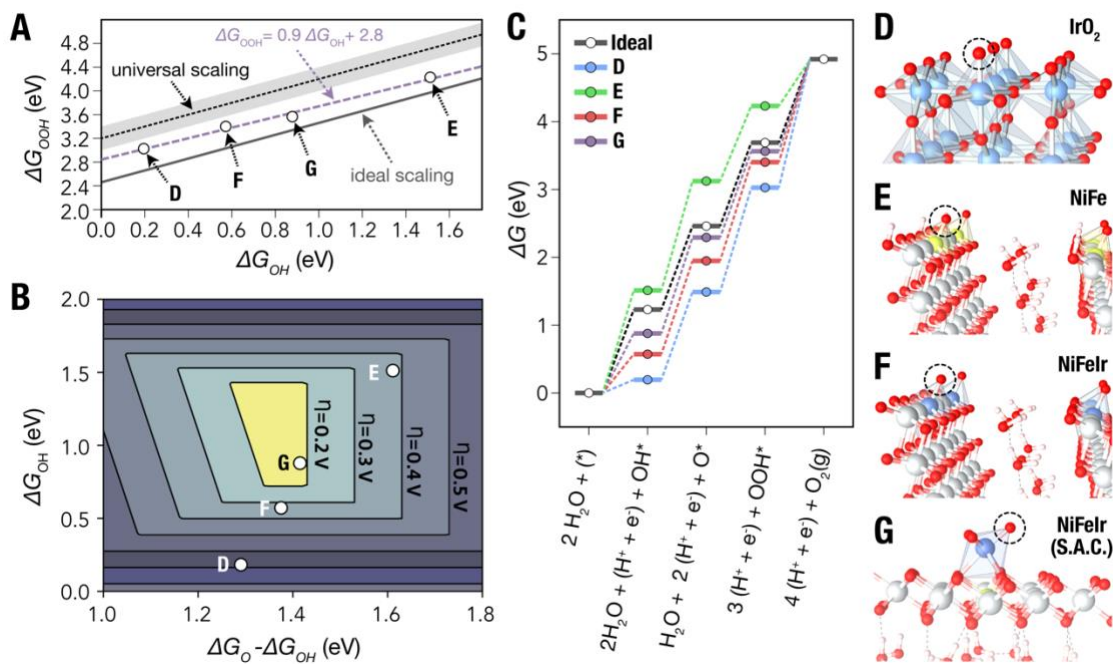


**Fig. 4 | Tuning the OER energetics of NiFeOOH via Ir site engineering.** (A) Improved  $\Delta G_{\text{OOH}}$  to  $\Delta G_{\text{OH}}$  (OH-OOH) scaling ( $\Delta G_{\text{OOH}} = \Delta G_{\text{OH}} + 2.686 \text{ eV}$ ) for the (d-g) models relative to the universal and ideal scaling lines. (B) Two-dimensional activity volcano plot with optimal region (shown in yellow) based on the (A) scaling and with positions of the thermodynamics for (D-G) systems. (C) Free energy diagram of the OER mechanism of our models relative to ideal catalyst (at  $U=0 \text{ V}$ ) highlighting the close similarity with model (G). (D-G) Structural models: (D) (110) surface of rutile- $\text{IrO}_2$  ( $\text{IrO}_2$ ), (E) (100) surface of  $\text{NiFe}$ , (F) Ir-site in the (100) surface of  $\text{NiFeIr}$ , and (G) (001) basal plane of  $\text{NiFeIr}$  SAC. Results for additional tested structures are shown in **Fig. S9**. All structures are shown with the  $\text{O}^*$  as adsorption intermediate. The atom colors are Ir (light-blue), Fe (yellow), Ni (light-grey), (O) red and H (light-pink), respectively.